RSC Advances

PAPER

View Article Online
View Journal | View Issue

Open Access Article. Published on 08 September 2025. Downloaded on 10/28/2025 4:06:54 PM.
This article is licensed under a Creative Commons Attribution-NonCommercial 3.0 Unported Licence.

Check for updates

Cite this: *RSC Adv.*, 2025, **15**, 32248

# Comprehensive structural and electrical characterization of lithium metavanadate for advanced lithium-ion battery cathodes

Leila Miladi,[a] Saber Nasri,[*ab] Amnah M. Alofi,[c] Manel Essid[d] and Abderrazek Oueslati[a]

Lithium metavanadate ($LiVO_3$) is a material of growing interest due to its monoclinic *C*2/*c* structure, which supports efficient lithium-ion diffusion through one-dimensional channels. This study presents a detailed structural, electrical, and dielectric characterization of $LiVO_3$ synthesized *via* a solid-state reaction, employing X-ray diffraction (XRD), scanning electron microscopy with energy-dispersive X-ray spectroscopy (SEM-EDS), and impedance/dielectric spectroscopy across a temperature range of 473–673 K and frequency range of 10 Hz to 1 MHz. XRD and Rietveld refinement confirmed high crystallinity and single-phase purity with lattice parameters $a = 10.155$ Å, $b = 8.421$ Å, $c = 5.881$ Å, and $\beta = 110.45°$. XRD confirmed single-phase purity and lithium stoichiometry, while SEM-EDS verified the uniform distribution of vanadium and oxygen, supporting chemical homogeneity. Impedance spectroscopy revealed thermally activated conduction with distinct grain (0.86 eV) and grain boundary (0.77 eV) activation energies, modeled using an equivalent circuit with constant phase elements, highlighting significant microstructural effects. AC conductivity follows Jonscher's universal power law, driven by a single-polaron hopping mechanism with strong electron-phonon coupling. Dielectric analysis showed pronounced non-Debye relaxation and space-charge polarization, influenced by temperature, frequency, and grain boundaries. These results elucidate the critical role of microstructure in governing charge transport and dielectric relaxation in $LiVO_3$, supporting its potential as a candidate material for lithium-ion battery cathodes. Targeted doping and interface engineering are proposed as promising future strategies to enhance its electrochemical properties, thereby advancing its applicability in energy storage research.

Received 5th August 2025
Accepted 2nd September 2025

DOI: 10.1039/d5ra05714k

rsc.li/rsc-advances

## 1 Introduction

The increasing global reliance on portable electronics, electric vehicles (EVs), renewable energy storage, and grid-scale power management systems continues to drive rapid development in lithium-ion battery (LIB) technologies. As the demand for cleaner, more efficient, and longer-lasting energy storage systems intensifies, significant efforts are directed toward improving key battery performance parameters—including energy density, cycle life, thermal stability, and cost-effectiveness.[1–4] These factors are particularly critical for next-generation EVs and large-scale energy storage applications, where high performance, safety, and affordability must be balanced.

Among the various components of LIBs, the cathode material is widely recognized as the most crucial determinant of energy density, voltage profile, and overall electrochemical performance. Consequently, an enormous body of research has been devoted to identifying and optimizing advanced cathode materials with high specific capacity, excellent rate capability, and long-term structural stability. Current candidates include Li-rich layered oxides, polyanionic frameworks (*e.g.*, phosphates and silicates), fluorinated compounds, and various transition metal oxides, particularly those based on vanadium.[5–7]

Vanadium-based oxides have garnered increasing attention in recent years due to their rich redox chemistry, variable oxidation states ($V^{3+}$, $V^{4+}$, $V^{5+}$), and flexible coordination environments. These properties facilitate the formation of a wide range of open-framework structures with tunable electronic and ionic transport characteristics. Moreover, vanadium oxides often exhibit relatively low cost, earth-abundance, and environmental compatibility, making them strong contenders for large-scale, sustainable battery systems.[8,9] The ability of

[a]*Laboratory of Spectroscopic Characterization and Optical Materials, Faculty of Sciences, University of Sfax, B.P. 1171, 3000 Sfax, Tunisia. E-mail: nasri.saber.1@gmail.com*

[b]*University of Gafsa, Preparatory Institute for Engineering Studies of Gafsa, El Khayzorane Street - Zaroug, Gafsa - 2112, Tunsia*

[c]*Physics Department, College of Science, Al-Baha University, Al Baha, 1988, Saudi Arabia*

[d]*Chemistry Department, College of Science, King Khalid University (KKU), Abha 61413, P.O. Box 9004, Saudi Arabia*

 © 2025 The Author(s). Published by the Royal Society of Chemistry

Open Access Article. Published on 08 September 2025. Downloaded on 10/28/2025 4:06:54 PM. This article is licensed under a Creative Commons Attribution-NonCommercial 3.0 Unported Licence.

vanadium to accommodate multiple lithium ions during cycling without significant structural degradation also adds to its appeal.[10]

Among the family of vanadium oxides, lithium metavanadate ($LiVO_3$) is an emerging cathode material that offers several compelling features. Crystallizing in the monoclinic system (space group $C2/c$), $LiVO_3$ is composed of one-dimensional chains formed by corner-sharing $VO_4$ tetrahedra and edge-sharing $LiO_6$ octahedra aligned along the $c$-axis. This structural arrangement provides efficient lithium-ion diffusion channels and contributes to its high theoretical specific capacity and reasonable cycling stability.[11,12] Unlike other layered vanadium oxides such as $LiV_2O_5$ and $LiV_3O_8$, $LiVO_3$ exhibits better structural integrity during charge/discharge cycles and can be synthesized more easily *via* scalable solid-state routes.[13]

Despite these advantages, $LiVO_3$ is not without its challenges. It tends to operate at lower voltages compared to other cathode candidates, which can limit its practical energy density. Additionally, like many transition metal oxides, it is susceptible to capacity fading over extended cycling due to lattice distortions, phase transitions, and interfacial instability.[14] To overcome these limitations, several strategies have been proposed, including cation doping (*e.g.*, $Al^{3+}$, $Mg^{2+}$, or $Ti^{4+}$ substitution), carbon or graphene coating, surface passivation, and nanostructuring, all aimed at enhancing lithium transport kinetics and improving electrode stability.[15]

Moreover, recent studies have emphasized the critical role of synthesis conditions—including temperature, atmosphere, precursors, and reaction time—in controlling the final morphology, particle size, crystallinity, and electrochemical behavior of vanadium-based oxides. For example, ultrasonic-assisted chemical synthesis has been employed to produce $LiVO_3$ nanorods with enhanced lithium storage behavior due to increased surface area and ion diffusion pathways. Hydrothermal routes yield nanoscale $LiVO_3$ structures with improved electrochemical kinetics. Sol–gel methods allow porous morphologies offering superior rate capabilities. Post-synthesis treatments like vacuum annealing influence structural stability and lithium mobility. Meanwhile, cation doping strategies have been demonstrated to optimize electrochemical performance by modifying structure and defects. These findings underscore the importance of fine-tuning synthesis routes to optimize performance.[16–18]

At the same time, a deeper understanding of the structural defects and local environments in $LiVO_3$ is needed to fully exploit its potential. Defects such as oxygen vacancies, interstitials, and structural water can significantly influence the material's conductivity, charge-storage mechanism, and long-term stability. Advanced characterization techniques such as X-ray photoelectron spectroscopy (XPS), Fourier-transform infrared spectroscopy (FTIR), and Raman spectroscopy have proven invaluable in identifying these defects and correlating them with performance outcomes.[19]

While significant progress has been made on vanadium oxides like $V_2O_5$, $V_4O_9$, and $\gamma$-$LiV_2O_5$, $LiVO_3$ remains relatively underexplored, especially regarding its electrical transport behavior, high-temperature stability, and frequency-dependent dielectric response. Most studies have focused primarily on electrochemical aspects without delving into the material's electrical and dielectric characteristics, which are essential for understanding ionic transport mechanisms, relaxation phenomena, and potential multifunctional applications such as sensors or solid-state devices.[10,14]

To date, comprehensive impedance spectroscopy and dielectric analysis of $LiVO_3$ under variable thermal and frequency conditions are scarce. Such studies are critical for probing charge carrier mobility, grain boundary effects, defect-related relaxation, and hopping mechanisms in the material. Insights from these investigations can not only improve the practical usability of $LiVO_3$ in LIBs but also position it as a promising material for next-generation solid-state batteries and energy-harvesting devices.[14]

In this study, we aim to bridge existing gaps by systematically investigating $LiVO_3$ synthesized through an optimized solid-state reaction method. Our approach focuses on establishing a detailed correlation between synthesis conditions and resulting structural features using X-ray diffraction (XRD) and scanning electron microscopy (SEM). To evaluate the material's electrical behavior, we perform dielectric and impedance spectroscopy analyses over a wide range of frequencies and temperatures, enabling insight into conduction mechanisms, relaxation dynamics, and grain-boundary contributions. Furthermore, temperature-dependent conduction behavior is explored through fitting experimental data to established models. A comparative analysis with other vanadium oxide-based cathode materials is also conducted to assess and benchmark the electrochemical potential of $LiVO_3$.

Through this comprehensive approach, we seek to uncover the fundamental structure–property–performance relationships that govern $LiVO_3$'s behavior under realistic operating conditions. Our findings not only contribute to the advancement of $LiVO_3$ as a cathode material for lithium-ion batteries but also open up new directions for its application in multifunctional energy storage devices and electrically active ceramic systems.

## 2 Experimental details

The $LiVO_3$ compound was synthesized *via* a conventional solid-state reaction technique. Stoichiometric amounts of lithium carbonate ($Li_2CO_3$) and vanadium pentoxide ($V_2O_5$), both of analytical grade purity (>99.9%), were accurately weighed, thoroughly ground, and homogenized using an agate mortar and pestle. The homogeneous mixture was gradually heated in a platinum crucible under ambient atmosphere at 573 K for 8 hours with a heating rate of 5 K $min^{-1}$ to decompose $Li_2CO_3$ and expel $CO_2$. After cooling, the resultant powder was reground, pressed into cylindrical pellets of approximately 8 mm diameter and ~1.1 mm thickness using a uniaxial hydraulic press at a pressure of ~200 MPa, then sintered at 1073 K for 10 hours with the same heating rate. Intermediate regrinding and repressing were performed once to promote phase homogeneity and densification.

X-ray powder diffraction (XRD) patterns were recorded at room temperature using a Cu-K$\alpha$ radiation source ($\lambda$ = 1.5406

Open Access Article. Published on 08 September 2025. Downloaded on 10/28/2025 4:06:54 PM.
This article is licensed under a Creative Commons Attribution-NonCommercial 3.0 Unported Licence.

Å), with a scanning range of 10°–70° $2\theta$ and step size of 0.02°. Phase identification and crystalline structure refinement were conducted employing the Rietveld method using the FULLPROF software suite.

The microstructure and elemental distribution of the synthesized samples were examined by scanning electron microscopy (SEM) coupled with energy-dispersive X-ray spectroscopy (EDS) utilizing a Zeiss EVO LS10 instrument. Samples were coated with a thin carbon layer prior to imaging to improve conductivity.

Impedance spectroscopy measurements were conducted over a frequency range of 10 Hz to 1 MHz and temperature range from 300 K to 573 K using a Solartron 1260 Impedance/Gain-Phase analyzer equipped with a high-temperature sample holder. The pellet surfaces were coated with a thin, uniform layer of silver paste, which was air-dried at room temperature to ensure good electrical contact and serve as blocking electrodes during measurements. Temperature ramp rates for electrical measurements were maintained at 2 K $min^{-1}$, with stabilization at each setpoint for 10 minutes before data acquisition to ensure thermal equilibrium.

# 3 Results and discussion

## 3.1. Powder X-ray diffraction (XRD)

The X-ray diffraction (XRD) pattern of the synthesized $LiVO_3$ sample, shown in Fig. 1(a), exhibits sharp and intense diffraction peaks, indicating high crystallinity. The diffraction data confirm that the sample crystallizes in a monoclinic system with the $C2/c$ space group. Rietveld refinement performed at room temperature yielded lattice parameters of $a = 10.155(2)$ Å, $b = 8.421(2)$ Å, $c = 5.881(1)$ Å, and $\beta = 110.45(1)$ °, in excellent agreement with previously reported crystallographic data.[20] The refinement quality is confirmed by the reliability factors: $R_p = 12.3\%$, $R_{wp} = 14.5\%$, $R_{exp} = 7.21\%$, and $\chi^2 = 2.48$, indicating an accurate fit and high phase purity. No additional peaks corresponding to impurity phases were observed, confirming the successful synthesis of single-phase $LiVO_3$.

## 3.2. Morphological characterization

The surface morphology, particle size, and distribution of the $LiVO_3$ sample were investigated using scanning electron microscopy (SEM), as illustrated in Fig. 1(b). This image reveals a highly crystalline structure characterized by elongated,

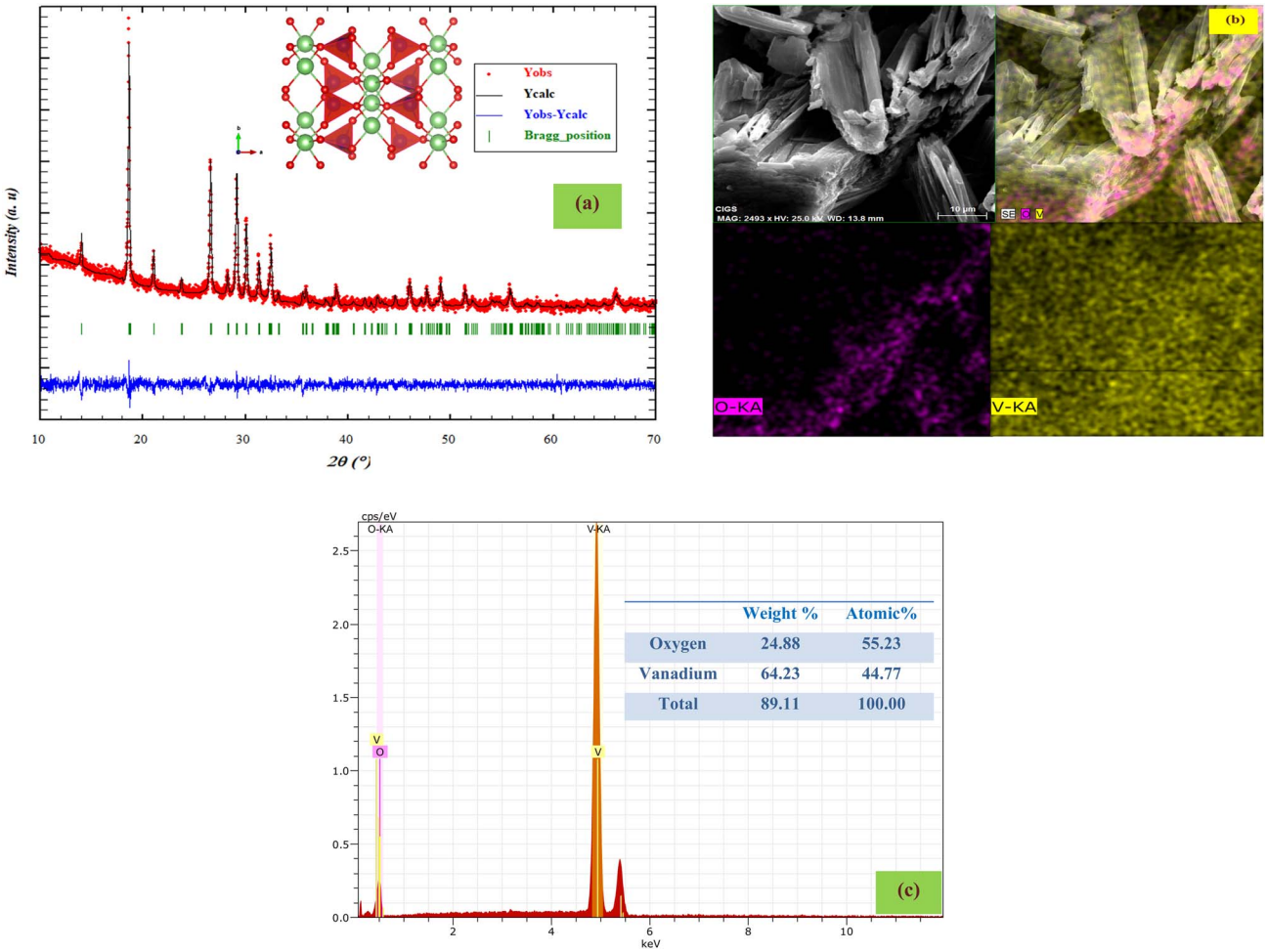


Fig. 1 (a) Powder X-ray diffractogram of $LiVO_3$ recorded at room temperature. The inset shows the crystal structure of the $LiVO_3$. (b) Morphological analysis of $LiVO_3$ by SEM imaging. (c) Energy-dispersive X-ray (EDX) spectrum and elemental composition analysis.

 © 2025 The Author(s). Published by the Royal Society of Chemistry

Open Access Article. Published on 08 September 2025. Downloaded on 10/28/2025 4:06:54 PM. This article is licensed under a Creative Commons Attribution-NonCommercial 3.0 Unported Licence.

needle-like formations, indicative of a well-defined growth pattern during synthesis. The rough texture and fibrous appearance suggest a high surface area, which is critical for applications such as lithium-ion battery electrodes or catalytic materials, as it facilitates enhanced ion diffusion and reactivity. The particle size appears relatively uniform, with the needle-like structures varying in length, potentially influencing the material's electrochemical performance.[21]

A key finding in this study is the pronounced agglomeration tendency observed among the grains. This agglomeration, specific to our synthesis protocol, directly impacts the material's microstructure and, consequently, its grain boundary resistance and charge carrier transport—factors that are critically relevant for optimizing electrical and electrochemical performance in battery applications. Such a microstructural profile suggests potential for tuning electrical pathways to enhance functional device properties, highlighting the novelty of the synthesis approach.

Elemental mapping by EDX (Fig. 1(c)) confirmed homogeneously distributed vanadium and oxygen, attesting to the phase purity and compositional uniformity of the sample. Of particular importance is the absence of extraneous elements, evident in the clean spectrum, which underlines the efficacy of the synthesis in achieving a single-phase product crucial for reliable battery operation. While lithium atoms were undetected due to their low atomic number and EDX sensitivity limitations,[22] their presumed even distribution is consistent with successful stoichiometric control—a novelty aspect that increases confidence in using $LiVO_3$ in advanced energy storage devices.

### 3.3. Impedance analysis

Impedance spectroscopy allows the distinction of electrical responses from various microstructural areas, including bulk grains, grain boundaries, and electrode interfaces, providing valuable understanding of the material's electrical properties.[23] In the case of $LiVO_3$, the Nyquist plots ($-Z''$ *versus* $Z'$) presented in Fig. 2(a) exhibit flattened semicircular whose centers lie beneath the real axis. This depression and deviation from ideal Debye behavior indicate a distribution of relaxation times arising from in homogeneities such as grain boundary effects, defects, and microstructural disorder.[24] This non-ideal behavior is a hallmark of polycrystalline ceramics and is consistent with the porous microstructure and agglomerated grains observed in SEM analysis.

The observed shrinkage of the semicircle diameter and corresponding decrease in real-axis intercept with increasing temperature are definitive signatures of thermally activated conduction processes. This trend highlights enhanced charge carrier mobility. It likely results from the reduction of electrostatic barriers at grain boundaries and increased hopping or interstitial diffusion within the bulk grains. Such temperature-dependent behavior reflects the semiconducting nature of $LiVO_3$, where electrical conductivity is intrinsically linked to thermal excitation of lithium ions and electrons/holes associated with vanadium valence states.[25,26] It is important to note that our electrical and dielectric spectroscopy results are intended to provide fundamental mechanistic insights into conduction and relaxation processes in $LiVO_3$ rather than directly simulating practical lithium-ion battery operating conditions.

To quantitatively model these phenomena, an equivalent circuit comprising: a parallel arrangement of grain resistance ($R_g$), grain capacitance ($C_g$), and a constant phase element (CPEg) representing distributed capacitance due to grain microstructure, in series with a parallel arrangement of grain boundary resistance ($R_{gb}$) and its associated CPE ($CPE_{gb}$), was employed. The excellent fit between experimental data and this circuit model (Fig. 2(a)) validates the interpretation that both grain and grain boundary effects significantly influence the overall electrical response.

An intriguing observation is the increase in both grain and grain boundary resistances with temperature (Fig. 2(b)), which diverges from typical metallic or ionic conductor behavior but aligns well with thermally activated semiconductors exhibiting defect-modulated conduction pathways.[27] This phenomenon may be linked to oxygen vacancy dynamics, where post-synthesis annealing reduces vacancy concentration, increasing activation energy barriers for conduction (measured here as 1.01 eV, Fig. 2(b) (inset)). The elevated activation energy indicates that electrical conduction primarily occurs through hopping between localized states associated with defect centers, specifically oxygen vacancies and vanadium oxidation state fluctuations.[12]

Dielectric spectroscopy reveals compelling features that further elucidate charge transport and polarization mechanisms. The capacitance–frequency profiles (Fig. 2(c)) demonstrate an increase in low-frequency capacitance with temperature, accompanied by enhanced dispersion. This phenomenon is generally explained by space charge polarization, where charges accumulate at grain boundaries and interfaces; this effect intensifies as increased thermal energy enhances carrier mobility. The linear decrease in capacitance at intermediate frequencies corresponds to diminishing space charge effects, while near-zero capacitance at high frequencies reflects the inability of slower polarization processes to follow the alternating field, leading to a temperature-independent high-frequency dielectric response.[28,29]

The bulk DC conductivity ($\sigma_{dc}$) of $LiVO_3$ was extracted from impedance spectroscopy measurements by using the bulk resistance ($R$) obtained from the equivalent circuit fitting, with the following relation:[30]

$$\sigma_{dc} = \frac{e}{RS} \tag{1}$$

where $e$ is the pellet thickness, S is the electrode area, and $R$ is the bulk resistance. The temperature dependence of $\sigma_{dc}$ demonstrates a clear Arrhenius-type behavior, described by:

$$\sigma_{dc} * T = A \exp\left(\frac{-E_a}{k_B T}\right) \tag{2}$$

where $E_a$ is the activation energy for conduction, $A$ is the pre-exponential factor and $k_B$ is Boltzmann's constant.

Open Access Article. Published on 08 September 2025. Downloaded on 10/28/2025 4:06:54 PM.
This article is licensed under a Creative Commons Attribution-NonCommercial 3.0 Unported Licence.

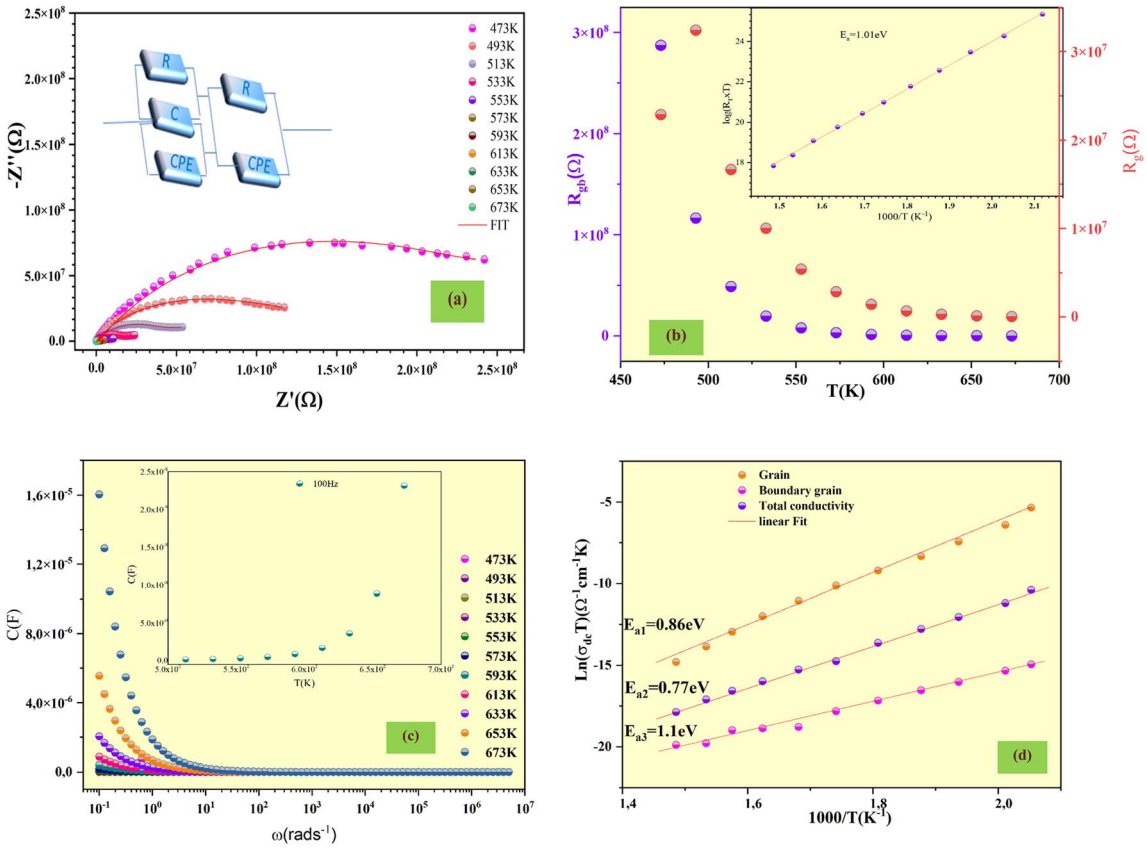


Fig. 2 (a) Nyquist plot with equivalent circuit representation of $LiVO_3$. (b) Temperature dependence of grain ($R_g$) and grain boundary ($R_{gb}$) resistances (inset: plot of ln($R_{gb}$/$T$) *vs.* 1000/$T$). (c) Frequency dependence of capacitance at different temperatures. (d) Variation of ln($\sigma_{dc}$) as a function of temperature.

From the Arrhenius plots (Fig. 2(d)), activation energies for conduction were determined as approximately 0.86 eV for grain (bulk), 0.77 eV for grain boundary, and 1.1 eV for the overall conductivity. The comparatively higher activation energy for overall conduction, relative to individual grain and grain boundary conduction values, highlights the significant influence of grain boundaries and interfaces in impeding charge transport across the bulk material.[31,32] This separation of grain and grain boundary resistances—a seldom addressed aspect in previous $LiVO_3$ literature—emphasizes the critical role of microstructural control and defect engineering in governing charge mobility.

The observed thermally activated conduction mechanism is consistent with ionic hopping of lithium cations through the one-dimensional channels formed by corner-sharing $VO_4$ tetrahedra and edge-sharing $LiO_6$ octahedra within the monoclinic $LiVO_3$ lattice. The dimensions and connectivity of these diffusion tunnels, alongside the polarizability of lithium ions and redox flexibility of vanadiumspecies ($V^{3+}/V^{4+}/V^{5+}$), facilitate the mixed ionic-electronic conduction critical for battery applications.[33]

Together, these electrical and dielectric findings not only confirm the inherent semiconductor character of $LiVO_3$ but also shed light on the critical roles of microstructure, defect chemistry, and interfacial phenomena. The pronounced grain boundary contribution is particularly significant, as it suggests that optimizing grain boundary composition, morphology, or introducing targeted dopants could substantially enhance electrical conductivity and reduce capacity fading during battery cycling.

### 3.4. Electrical conductivity analysis

The AC conductivity ($\sigma_{ac}$) of $LiVO_3$, as depicted in Fig. 3(a), demonstrates a pronounced frequency dependence that can be clearly divided into two distinct regimes corresponding to different conduction pathways in the material. At lower frequencies, the conductivity profile exhibits a near-constant plateau, which we attribute primarily to the grain boundary response. Grain boundaries in polycrystalline ceramics often act as resistive barriers or trapping regions that impede charge carrier mobility, resulting in suppressed conductivity at low frequencies where carriers have sufficient time to interact and become localized. This behavior leads to the formation of space charge regions and ionic atmospheres at grain boundaries, contributing to charge accumulation and polarization effects that dominate the low-frequency response. The relative invariance of conductivity in this regime suggests that charge carriers encounter steady, frequency-independent barriers associated with these microstructural features.

 © 2025 The Author(s). Published by the Royal Society of Chemistry

Open Access Article. Published on 08 September 2025. Downloaded on 10/28/2025 4:06:54 PM.
This article is licensed under a Creative Commons Attribution-NonCommercial 3.0 Unported Licence.

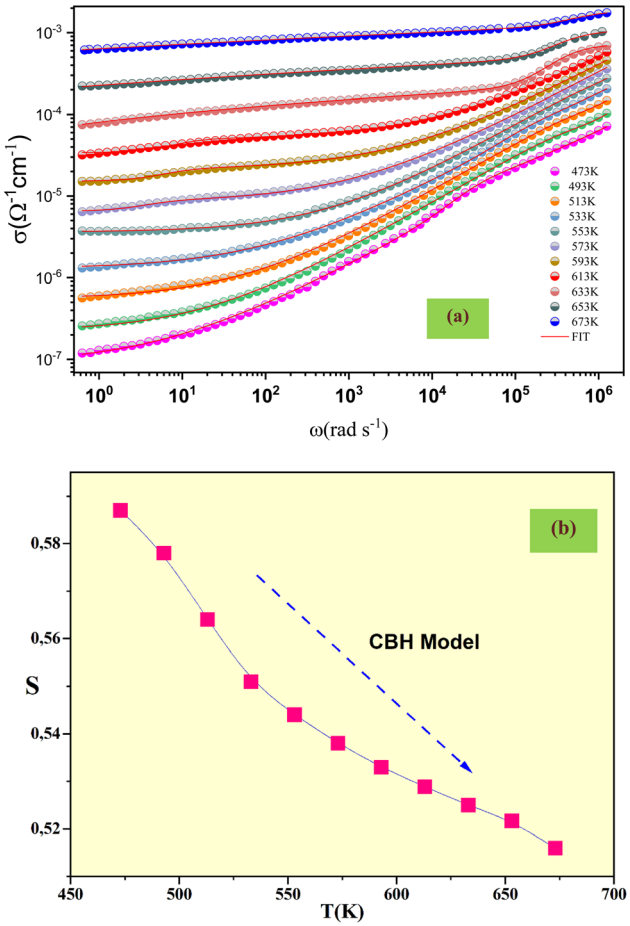


Fig. 3 (a) Frequency dependence of the ac conductivity at various temperatures. (b) Temperature dependence of the frequency exponent s.

Conversely, at higher frequencies, conductivity increases progressively with frequency, indicating a transition to grain (bulk) dominated conduction. This dispersive behavior arises because, at increased frequencies, the alternating electric field oscillates rapidly enough to enable charge carriers to hop or tunnel between localized states within the grains before they are impeded by grain boundary barriers. Such frequency-dependent conductivity reflects the dynamic relaxation of the ionic atmosphere surrounding charge carriers, a process rooted in their ability to respond to varying electric fields through hopping and reorientation. This relaxation reduces the effective impedance to carrier motion, enabling enhanced conduction within the grains at elevated frequencies.

The dual nature of this AC conductivity behavior—frequency-independent plateau at low frequencies transitioning to frequency-dependent dispersion at high frequencies—is hallmark evidence of the heterogeneous electrical environment in $LiVO_3$. It neatly illustrates the coexistence of microstructural influences, where grain boundaries act as bottlenecks at low frequencies, while intrinsic grain properties govern conduction at higher frequencies.[34]

Importantly, this frequency dependence aligns with Jonscher's universal power law, which mathematically captures such behavior in a wide class of disordered and polycrystalline materials. The power law is expressed as:[35]

$$\sigma_{ac}(\omega) = \frac{\sigma_s}{1+\tau^2\omega^2} + \frac{\sigma_\infty \tau^2\omega^2}{1+\tau^2\omega^2} + A\omega^s \quad (3)$$

where $\sigma_s$ represents the conductivity in the lower frequency range, while $\sigma_\infty$ estimates conductivity at the higher frequency range. The parameter $\tau$ denotes the typical relaxation time, $A$ is a constant temperature dependent, and $s$ denotes the power law exponent, which indicates the strength of the interaction between the environment and mobile ions. In $LiVO_3$, the increase in conductivity with frequency (observed at frequencies above the grain boundary dominated regime) closely follows this power law, indicating relaxation processes governed by hopping conduction.

Physically, the exponent $s$ embodies the dynamics of charge carrier hopping over potential barriers or between localized states whose distribution is influenced by structural disorder, defects, and microstructural features such as grain boundaries and porosity. As frequency increases, carriers access more pathways with reduced impedance *via* hopping, leading to the observed conductivity enhancement. Additionally, the ionic atmosphere—representing the local polarization fields and space charge regions around an ion—relaxes more rapidly under high-frequency excitation, facilitating ionic hopping which manifests as frequency-dependent dispersion.

To further elucidate the conduction mechanism, we analyzed the temperature dependence of the power-law exponent $s$. Several theoretical models have been developed to elucidate AC conductivity mechanisms in disordered materials. These include the Correlated Barrier Hopping (CBH), Non-Overlapping Small Polaron Tunneling (NSPT), Overlapping Large Polaron Tunneling (OLPT), and Quantum Mechanical Tunneling (QMT) models. Each predicts a characteristic temperature dependence of $s$: CBH predicts a decrease of $s$ with temperature, NSPT an increase, OLPT a non-monotonic trend, and QMT a nearly temperature-independent $s$ near 0.8.[36] As detailed later, our experimental results show a systematic decrease in $s$ with increasing temperature, which is characteristic of the CBH model Fig. 3(b). This suggests that charge transport occurs *via* thermally assisted hopping over correlated energy barriers, likely associated with structural disorder and defect states in the $LiVO_3$ matrix$_3$. Drawing on the Correlated Barrier Hopping (CBH) model, the electrical conductivity in $LiVO_3$ is primarily driven by the thermally activated movement of charge carriers, such as electrons or polarons, between localized defect states or sites within the crystal lattice. In this model, charge carriers must surmount distinct coulombic energy barriers linked to structural defects or trap centers to transition between these sites. Initially proposed by Pike in 1972 to explain single-electron hopping, the CBH model was later refined by Elliot in 1977 to include the simultaneous hopping of two electrons, known as bipolarons.[37]

Open Access Article. Published on 08 September 2025. Downloaded on 10/28/2025 4:06:54 PM.
This article is licensed under a Creative Commons Attribution-NonCommercial 3.0 Unported Licence.

To describe the AC conductivity and derive the power-law exponent $s$ in the (CBH) model, the following equation is employed:

$$s(T) = 1 - \left(\frac{6k_B T}{W_M + k_B T \ln(\omega\tau_0)}\right) \quad (4)$$

Here, $W_M$ denotes the energy required to move a charge carrier from one site to another, $\tau_0$ denotes the characteristic relaxation time, and $k_B$ is Boltzmann's constant. When in the specific case where $W_M \gg k_B T \ln(\omega\tau_0)$, the equation reduces to:

$$s(T) = 1 - \left(\frac{6k_B T}{W_M}\right) \quad (5)$$

This simplified form illustrates that the value of $s(T)$ decreases linearly with increasing temperature, with the slope determined by the ratio of 6 $k_B$ to the binding energy $W_M$. This relationship is central to the CBH model, as it highlights the role of thermal activation and the energy barrier in the hopping process.

The electrical conductivity according to CBH model is described by:[38]

$$\sigma_{ac} = \frac{n\pi^3 \varepsilon\varepsilon_0 \mathrm{NN_p} \omega R_\omega{}^4}{24} \quad (6)$$

In these expressions, $e$ represents the electronic charge, $R_\omega$ stands for the hopping distance, $\varepsilon$ and $\varepsilon_0$ are the dielectric constants of the material and free space, respectively, NNp is directly related to the square of the concentration of states, and $n$ indicates the number of participating electrons, with $n = 1$ corresponding to single-polaron hopping and $n = 2$ for bi-polaron hopping.

Within the CBH framework, the polaron population $\mathrm{NN_p}$ depends on the hopping mechanism as follows:

$\mathrm{NN_p} = N \cdot T^2$(for bipolaron hopping).

$\mathrm{NN_p} = N \cdot T^2 \exp(-U_{eff}/2kT)$ (For single-polaron hopping).

Where $N$ is a proportionality constant representing the effective density of localized hopping sites available for conduction, and $U_{eff}$ is the effective Coulomb repulsion energy that acts as an energetic barrier reducing the number of free polarons able to hop.

Moreover, $R_\omega$ can be presented by:

$$R_\omega = \left(\frac{4e^2}{\varepsilon'[W + kT \ln(\omega\tau)]}\right) \quad (7)$$

Fig. 4(a) illustrates the variation of AC conductivity ($\ln(\sigma_{ac})$) as a function of inverse temperature ($1000/T$) for the $LiVO_3$ sample. The AC conductivity is well-described by a single conduction mechanism involving single-polaron hopping. The theoretical values (represented by lines) closely match the experimental data (shown as symbols), indicating that this model provides a straightforward and effective approach to capturing the approximate frequency dependence of AC conductivity. The variables involved in the fitting procedure are detailed in Table 1. The negative effective energy suggests a strong electron-phonon interaction.

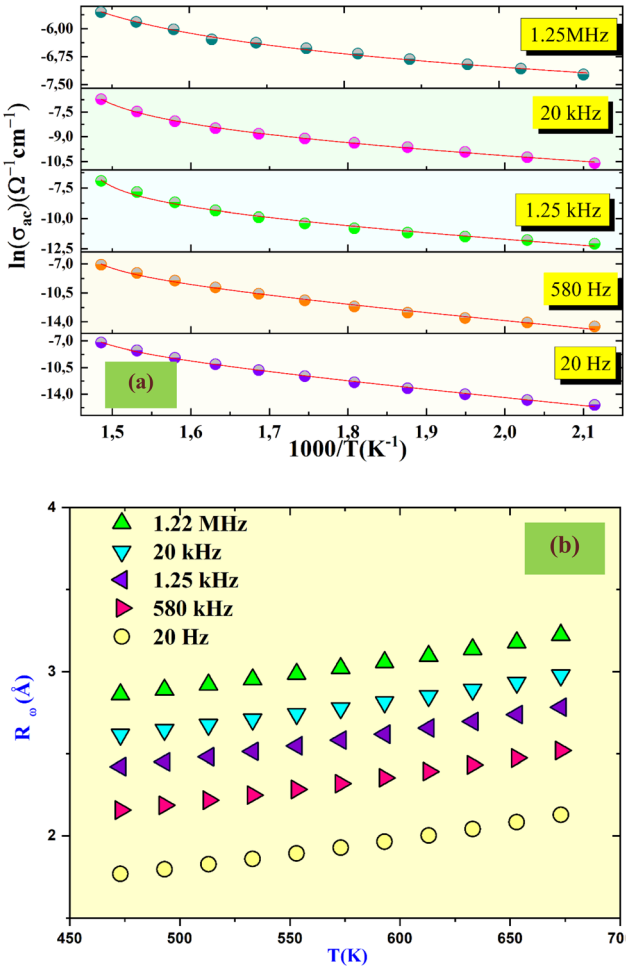


Fig. 4 (a) AC conductivity of $LiVO_3$ *vs.* $1000/T$ at various frequencies, fitted to the correlated barrier hopping (CBH) model. (b) The temperature dependence of $R_\omega$ (Å) of $LiVO_3$ at different indicated frequencies.

Depicted in Fig. 4(b) is the temperature-dependent behavior of the hopping distance $R_\omega$ across various frequencies, as derived from the CBH mode. The estimated hopping distances (~3.2–3.35 Å) closely correspond to the Li–Li interatomic distances within the crystal lattice, confirming that charge carriers predominantly hop between adjacent lithium sites coordinated by oxygen ions. This empirical finding aligns well with theoretical and experimental studies demonstrating that small polaron hopping in transition metal oxides (TMOs) typically occurs over metal–oxygen–metal interatomic distances.[39,40]

Table 1 AC conductivity parameters at various frequencies

| | Frequency (KHz) | $U_{eff}$ (eV) | $\varepsilon'$ | $N(E_F)$ ($eV^{-1}\ m^{-3}$) | $W_m$ (eV) |
|---|---|---|---|---|---|
| CBH model | 0.020 | −0.0037 | 0.66 | $1.1 \times 10^{16}$ | 0.41 |
| | 0.580 | −0.0029 | | $8.9 \times 10^{16}$ | |
| | 1.25 | −0.0020 | | $6.8 \times 10^{17}$ | |
| | 20 | −0.0010 | | $8.7 \times 10^{20}$ | |
| | 1250 | −0.0009 | | $9.7 \times 10^{22}$ | |

 © 2025 The Author(s). Published by the Royal Society of Chemistry

Open Access Article. Published on 08 September 2025. Downloaded on 10/28/2025 4:06:54 PM. This article is licensed under a Creative Commons Attribution-NonCommercial 3.0 Unported Licence.

Importantly, the structural framework formed by interconnected $VO_4$ tetrahedra and $LiO_6$ octahedra not only defines the lithium migration pathways but also significantly influences polaron localization and hopping energetics due to local variations in the electronic environment and lattice distorsions (Table 2).

Within this framework, lithium ions occupy multiple crystallographically distinct sites, designated as Li0 through Li7, which collectively form a network of one-dimensional diffusion pathways aligned along specific crystallographic directions. These interconnected channels facilitate facile lithium-ion migration across the lattice by providing continuous conduction corridors characterized by relatively low migration energy barriers, thereby energetically favoring $Li^+$ ion hopping between adjacent interstitial or vacancy sites.

Embedded within a robust matrix of vanadium-oxygen octahedra, the crystal structure is further stabilized by mixed valence $V^{4+}/V^{5+}$ centers, which facilitate polaronic conduction that complements ionic transport. Moreover, the distortion characterized by the monoclinic angle $\beta \approx 111.5°$ modulates the connectivity and dimensionality of lithium diffusion channels, enhancing anisotropic ionic mobility. This anisotropy may result in direction-dependent conductivity, beneficial for targeted design and optimization of battery electrode materials. The presence of multiple lithium sites with distinct crystallographic environments also implies a distribution of site energies, enabling variable-range hopping conduction at elevated temperatures consistent with experimentally observed thermally activated transport mechanisms.

In addition to these intrinsic structural and electronic factors, the close spatial proximity of lithium sites within distorted octahedral and tetrahedral coordination polyhedra promotes strong coupling between ion migration and lattice vibrations. This dynamical interplay stabilizes polaron hopping and lithium diffusion through lattice relaxation processes, ultimately enhancing the overall electrochemical performance of $LiVO_3$ as a cathode material. Collectively, the well-defined monoclinic crystal architecture, combined with the congruence between hopping distances and lattice parameters demonstrated in Fig. 4(b), provides a compelling structural and mechanistic template for efficient lithium-ion conduction *via* reduce polaron hopping barriers in vanadates, potentially enhancing conductivity.[41]

Dielectric measurements reinforcing grain boundary relaxation phenomena corroborate the view that microstructure critically affects overall transport and suggests that dense, well-connected grains with minimal grain boundary resistance can significantly boost device performance. This is consistent with comparable studies on $LiFePO_4$ and $LiMn_2O_4$, where grain boundary engineering *via* sintering or coating markedly improves lithium conductivity.[42] Notably, dielectric constant values in $LiVO_3$, combined with the CBH model fitting parameters, allow quantification of hopping energetics that dovetail with structural bond lengths, providing a physically consistent picture of polaronic transport supported at the atomic scale.

In summary, our comprehensive conductivity analysis firmly positions $LiVO_3$ within the family of lithium transition metal oxides dominated by polaronic, hopping-based charge transport modulated by crystal structure and microstructural defects. Its anisotropic layered structure, multivalent vanadium chemistry, and pronounced grain boundary effects differentiate it from other TMOs but also offer tunable avenues for engineering improved electrical and ionic conductivities critical for next-generation lithium-ion battery cathodes.

### 3.5. Investigation of dielectric behavior

The electric modulus formalism is a powerful tool for investigating electrical transport mechanisms in solid-state materials,

Table 2 Comparative overview of $LiVO_3$ synthesis ethods, key features, and reported performance

| Synthesis method | Reference | Key parameters | Advantages/characteristics | Performance notes |
|---|---|---|---|---|
| Sol–gel | 60 | Annealing at 450 °C | Best electrochemical performance for LVO-450 | Optimal performance after annealing at 450 °C |
| Sol–gel (with sync-carbonization) | 61 | Simple evaporation approach, sync-carbonization | Simultaneous formation of carbon layer and $LiVO_3$ | Improved electrochemical performance due to carbon coating |
| Ball milling + solid-state reaction | 62 | Synthesis at 350 °C | Low crystallization, small particle size | Optimal performance at 350 °C, good cycling stability |
| Soft chemistry + calcinations | 63 | Fabrication at 350 °C | Small particles (500 nm to 1 μm) | Good performance, high discharge capacity, good rate capability and cyclic stability |
| Hydrothermal + $N_2$ annealing | 64 | Hydrothermal method, annealing under nitrogen atmosphere | Better performance than air-annealed $LiVO_3$ | Post-synthesis annealing under $N_2$ enhances properties |
| Solid-state reaction (this work) | This work | Heating at 573 K for 8 h, sintering at 1073 K for 10 h, intermediate grinding and pressing | High phase purity, monoclinic *C*2/*c* structure, needle-like morphology, controlled agglomeration | Thermally activated conduction, distinct grain/grain boundary activation, strong polaron hopping conductivity, favorable dielectric behavior for Li-ion batteries |

Open Access Article. Published on 08 September 2025. Downloaded on 10/28/2025 4:06:54 PM.
This article is licensed under a Creative Commons Attribution-NonCommercial 3.0 Unported Licence.

particularly for separating relaxation processes originating from grains (bulk), grain boundaries, and electrode–material interfaces. It also provides valuable insight into charge carrier dynamics, ion-hopping processes, and dielectric relaxation behavior.[43]

Mathematically, the complex electric modulus $M^*$ is defined as the inverse of the complex permittivity $\varepsilon^*$, and it can be calculated using the experimentally measured impedance data as follows:

$$M^*(\omega) = M' + jM'' = \omega C_0 Z'' + j\omega C_0 Z' \tag{8}$$

where $M'$ (real part) $= \omega C_0 Z''$, $M''$(imaginary part) $= \omega C_0 Z'$, $\omega =$ angular frequency $= 2\pi f$, $C_0 =$ geometrical capacitance $= \varepsilon_0 \times A/d$ ($\varepsilon_0 =$ permittivity of free space, $A =$ area of electrode surface, and $d =$ thickness).

Fig. 5 presents the complex modulus plot ($M''$ *versus* $M'$) for $LiVO_3$, showing two separate semicircular arcs that correspond to the relaxation processes of the bulk grains and the grain boundaries. This observation is consistent across the temperature range studied and matches the Cole–Cole semicircles seen in impedance spectra, confirming that both microstructural regions contribute significantly to the overall electrical behavior. Such behavior reflects a non-Debye relaxation mechanism, characterized by a distribution of relaxation times likely due to structural heterogeneities and defect states within the ceramic.

A more detailed investigation of the frequency dependence of the imaginary components of impedance and modulus, namely $-Z''(\omega)$ and $M''(\omega)$, allows for critical insights into the nature of charge carrier dynamics and relaxation type. When the peak frequencies of the impedance loss (denoted as $Z''_{max}$) and modulus loss ($M''_{max}$) coincide, this indicates a dominant long-range carrier motion consistent with ideal Debye relaxation and delocalized transport. However, a mismatch or frequency shift between these peaks reveals localized or short-range hopping conduction, characteristic of non-Debye relaxation.[44]

For $LiVO_3$, at elevated temperatures such as 653 K, a pronounced mismatch between $M''_{max}$ and $Z''_{max}$ peak frequencies is observed (see Fig. 6), signifying that polarons undergo short-range hopping rather than long-range conduction. This deviation from ideal Debye behavior highlights strong electron-phonon coupling and possible trapping or localization effects induced by microstructural defects or grain boundary potentials.[45]

The temperature-dependent frequency spectra of the imaginary electric modulus component $M''$ (Fig. 7(a)) show slightly asymmetric peaks that systematically shift to higher frequencies with increasing temperature. This behavior supports the ionic conductor character of $LiVO_3$, where ion mobility increases thermally. The frequency region to the left of the M″peak corresponds to ions exhibiting long-range transport, while to the right, ions remain spatially confined within potential wells.[46]

To quantitatively model this relaxation, the M″ data were fitted using the Kohlrausch–Williams–Watts (KWW) stretched exponential function, which characterizes relaxation with a stretching parameter $\beta$ between 0 and 1.

$$M'' = \frac{M''_{max}}{\left[(1-\beta) + \left(\frac{\beta}{1+\beta}\right)\right]\left[\beta\left(\frac{\omega_m}{\omega}\right) + \left(\frac{\omega}{\omega_m}\right)\right]^{\beta}} \tag{9}$$

Values of $\beta$ less than unity, as shown in Fig. 7(b), confirm strong dipole–dipole coupling and non-Debye relaxation behavior, indicative of interacting mobile ions and complex conduction pathways,[47,48] the dielectric response of $LiVO_3$ is further described by the complex permittivity:[49]

$$\varepsilon^* = \varepsilon' - j\varepsilon'' \tag{10}$$

where $\varepsilon'$ and $\varepsilon''$ are the real (dielectric constant) and imaginary (dielectric loss) components, respectively. Fig. 8 and 9 show that both $\varepsilon'$ and $\varepsilon''$ markedly increase at low frequencies, then gradually decline as frequency rises, eventually plateauing at

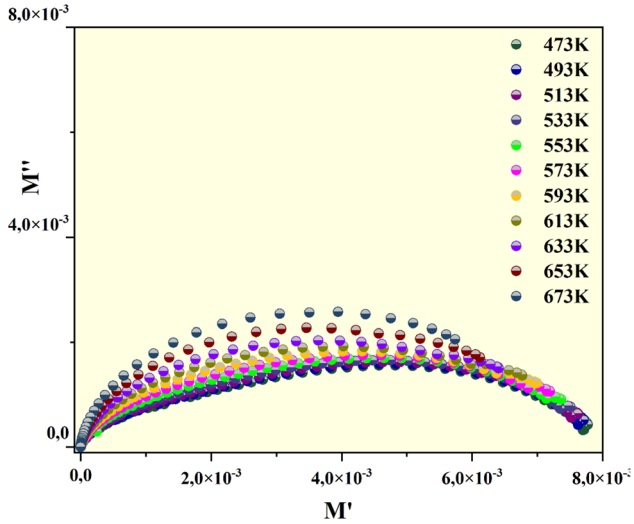


Fig. 5 Variation of $M''$ *vs.* $M'$.

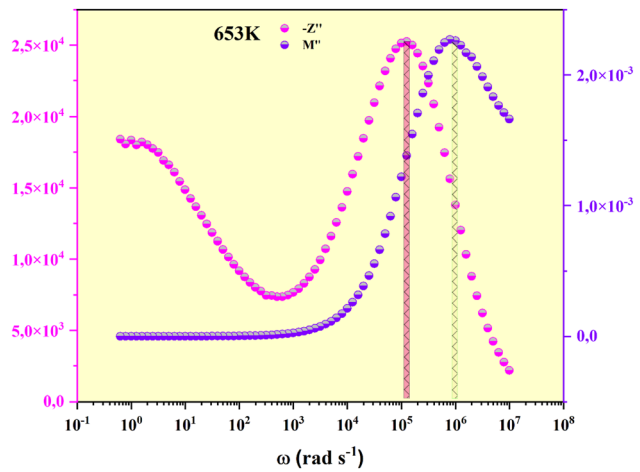


Fig. 6 Variation of $Z''$ and $M''$ with Frequency at 673 K for $LiVO_3$.

 © 2025 The Author(s). Published by the Royal Society of Chemistry

Open Access Article. Published on 08 September 2025. Downloaded on 10/28/2025 4:06:54 PM.
This article is licensed under a Creative Commons Attribution-NonCommercial 3.0 Unported Licence.

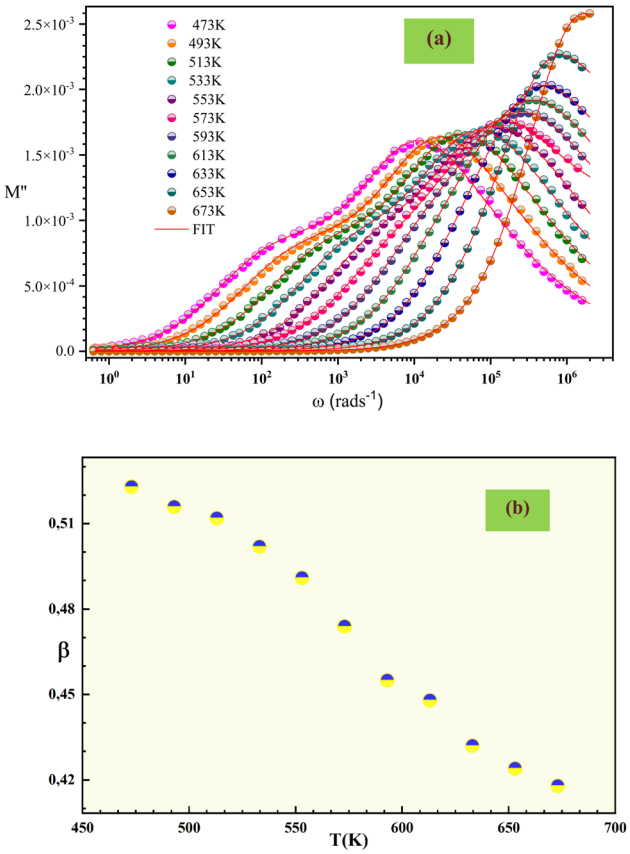


Fig. 7 (a) Frequency dependence of $M''$ at several temperatures. (b) Thermal evolution of $\beta$.

high frequencies. This frequency dependence reveals dielectric dispersion related to the inability of electronic and ionic dipoles within the grains to respond to rapidly alternating fields at higher frequencies.

This behavior is characteristic of dielectric dispersion caused by multiple polarization mechanisms. At low frequencies,

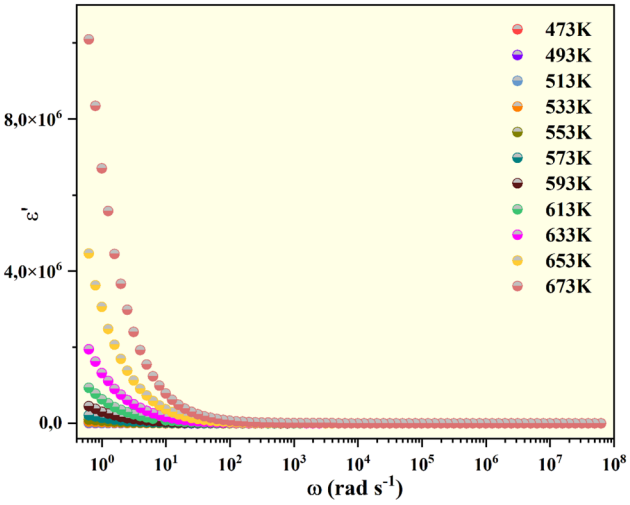


Fig. 8 Frequency dependence of $\varepsilon'$ at several temperatures.

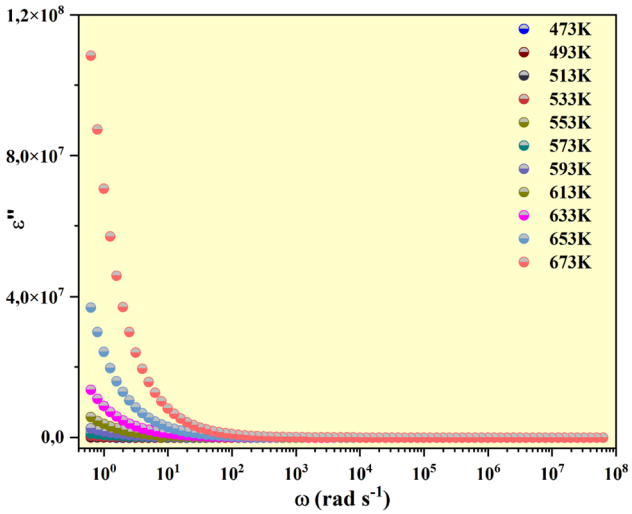


Fig. 9 Frequency dependence of $\varepsilon''$ at several temperatures.

space-charge and orientation polarizations dominate due to charge accumulation at grain boundaries and dipole alignment. The high dielectric constant at low frequencies underscores the Maxwell–Wagner interfacial polarization effect, where charge carriers hop between conductive grains separated by less conductive grain boundaries, effectively forming internal barrier layers analogous to multi-layer capacitors. As frequency increases, ionic and electronic polarizations become significant, but overall dielectric response diminishes as dipoles cannot follow rapid field oscillations. This multifaceted polarization behavior confirms complex microstructural influences on dielectric properties essential for battery cathode performance.[50,51]

In vanadate ceramics such as $LiVO_3$, the primary contributor to dielectric polarization is closely linked to the conduction mechanism within the material. Specifically, this phenomenon involves hopping conduction of $Li^+$ ions between localized sites, which induces polarization throughout the material matrix. This ion hopping not only facilitates charge transport but also leads to accumulation of charge at microstructural interfaces, such as grain boundaries, thus generating interfacial polarization.[52]

The Maxwell–Wagner interfacial polarization model aptly describes the observed dielectric behavior of our $LiVO_3$ sample and aligns well with Koop's phenomenological theory of dielectrics. According to Koop's model, the ceramic material can be considered as a microcomposite consisting of grains with relatively high electrical conductivity surrounded by grain boundaries exhibiting much lower conductivity.[53] At low frequencies, the highly conducting grains dominate the dielectric response because the charge carriers have sufficient time to accumulate at interfaces and contribute to polarization. Conversely, at higher frequencies, the grain boundaries, acting as resistive barriers, impede charge displacement and hence substantially influence the dielectric properties.[54]

In the sample under investigation, this microstructural arrangement thus mimics a multilayer capacitor, where

Open Access Article. Published on 08 September 2025. Downloaded on 10/28/2025 4:06:54 PM.
This article is licensed under a Creative Commons Attribution-NonCommercial 3.0 Unported Licence.

conducting grains form the plates and the less conductive grain boundaries act as dielectric layers. This model explains the strong frequency dependence of the dielectric constant, showing high values at low frequencies due to interfacial polarization effects, which gradually decrease as the frequency increases and polarization is suppressed.

Dielectric loss, represented by the loss tangent tan $\delta$, quantifies the electrical energy dissipated as heat within the dielectric material under an alternating electric field, and is critical for evaluating material efficiency in energy storage and transfer applications. The dielectric loss is mathematically related to both the real ($\varepsilon'$) and imaginary ($\varepsilon''$) components of the dielectric constant by the equation:[55]

$$\tan\delta = \frac{\varepsilon''}{\varepsilon'} \tag{11}$$

Fig. 10 presents the frequency dependence of the dielectric loss tangent (tan $\delta$) of $LiVO_3$ ceramic measured at various temperatures. The loss tangent decreases with increasing frequency, indicating the diminishing ability of charge carriers to follow rapidly oscillating electric fields at higher frequencies, thereby reducing dielectric energy dissipation. Conversely, tan $\delta$ increases with rising temperature due to thermally activated charge carriers that enhance ionic hopping and conduction mechanisms, leading to greater dielectric loss. This behavior reflects the complex interplay between charge carrier mobility and polarization mechanisms in the material.[56]

The observed frequency and temperature dependence of tan $\delta$ can be understood through the Maxwell–Wagner interfacial polarization model paired with Koop's phenomenological theory, which interprets the ceramic as consisting of highly conductive grains separated by grain boundaries exhibiting low conductivity. At low frequencies, charge carriers accumulate at grain boundaries due to their higher resistivity, resulting in increased dielectric loss. As frequency increases, these interfacial charges cannot respond quickly, causing a reduction in loss tangent. Temperature elevation increases the concentration and mobility of charge carriers, particularly through hopping of $Li^+$ ions, thereby enhancing energy dissipation.

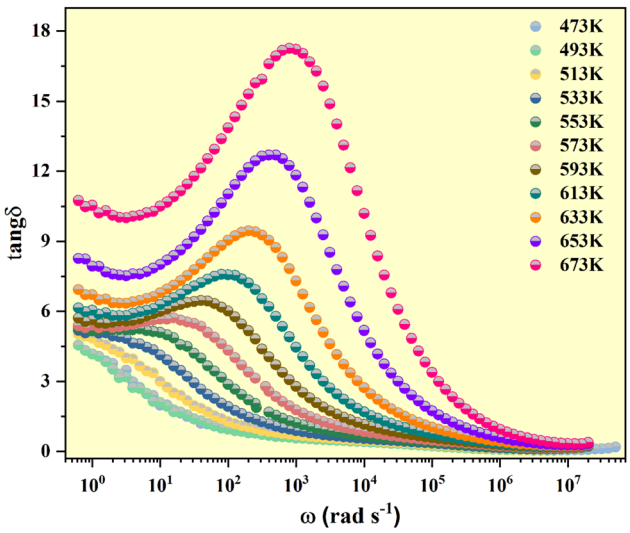


Fig. 10 Frequency dependence of tan($\delta$) at several temperatures.

These insights from Fig. 10 complement and reinforce the earlier observations from the dielectric constant and electric modulus analyses, which collectively highlight the non-Debye relaxation behavior dominated by grain and grain boundary heterogeneity. Understanding how tan $\delta$ evolves with frequency and temperature is crucial for optimizing $LiVO_3$ ceramics as lithium-ion battery cathodes, where balancing ionic conductivity and minimizing dielectric losses are key for improved electrochemical performance and energy efficiency.

Beyond these dielectric and conductivity insights, it is also important to place our results in the broader context of recent cathode material developments. Recent advances in layered and oxide-based cathodes demonstrate the importance of tailoring structure and electronic states to optimize energy storage performance. For instance, it has been reported that multiple cation substitution can induce an order-to-disorder transition, enabling quasi-zero-strain behavior in layered oxide cathodes.[57] In a related work, interlayer entropy engineering was shown to activate high-voltage redox reactions in symmetry-broken layered oxides.[58] Similarly, in aqueous zinc-ion systems, engineering the oxygen p-band center was found to significantly enhance proton intercalation in $\delta$-$MnO_2$.[59] These studies highlight innovative design strategies to optimize layered and manganese-based oxides for high-performance batteries.

By contrast, our work focuses on $LiVO_3$, a vanadium-based monoclinic oxide that has been relatively underexplored. Unlike the above strategies that rely on cation substitution or band-center engineering, our novelty lies in a systematic analysis of electrical transport and dielectric behavior in $LiVO_3$. Specifically, we quantify separate activation energies for grain (0.86 eV) and grain boundary (0.77 eV) conduction, reveal single-polaron hopping as the dominant AC conduction mechanism, and identify pronounced non-Debye relaxation linked to microstructural effects. These mechanistic insights, which have not been reported for $LiVO_3$, complement the structural and electrochemical engineering approaches developed for layered and Mn-based oxides. Together, such studies collectively enrich the understanding of cathode materials by combining structural design with fundamental transport and dielectric analysis.

The experimental results further demonstrate that the structural and functional properties of $LiVO_3$ strongly depend on synthesis conditions. Our solid-state synthesis—precursor heating at 573 K for 8 hours, followed by sintering at 1073 K for 10 hours with intermediate grinding and pressing—yields a high-purity monoclinic $C2/c$ phase with elongated needle-like morphology and controlled grain agglomeration. This method achieves robust electrical performance, evidenced by the quantified grain and grain boundary activation energies, pronounced polar on hopping conduction, and favorable dielectric responses. Compared with sol–gel or hydrothermal methods, which often produce smaller particle sizes and enhanced electrochemical cycling but require more complex,

 © 2025 The Author(s). Published by the Royal Society of Chemistry

Open Access Article. Published on 08 September 2025. Downloaded on 10/28/2025 4:06:54 PM.
This article is licensed under a Creative Commons Attribution-NonCommercial 3.0 Unported Licence.

costly, or time-consuming processing, the solid-state route offers a more economical, scalable, and reproducible pathway. It balances crystallinity, morphology control, and electrochemical relevance effectively, making it a practical synthesis choice.

Together, these results illustrate how combining fundamental transport and dielectric analysis with informed synthesis strategies provides a complementary perspective to structural and electrochemical design approaches in cathode materials.

## 4 Conclusion

In this work, $LiVO_3$ was successfully synthesized *via* the solid-state reaction method, and its structural, microstructural, and electrical properties were systematically investigated. XRD analysis confirmed the formation of a phase-pure material with well-defined crystallinity, while SEM observations revealed a homogeneous microstructure with interconnected grains. Impedance and conductivity studies demonstrated NTCR-type semiconducting behavior, where both grain and grain boundary contributions were evident, with grain boundary resistance consistently higher than grain resistance. The AC conductivity spectra revealed two distinct regimes corresponding to long-range and localized conduction processes, and the activation energies derived from Arrhenius analysis provided further insight into the thermally activated nature of ionic transport. Dielectric studies confirmed strong frequency and temperature dependence, characteristic of hopping and interfacial polarization mechanisms.

Importantly, this study highlights the intrinsic correlation between synthesis, structure, and functional properties. The solid-state reaction route employed here yielded phase purity and favorable grain connectivity, which directly influenced the impedance response and charge transport pathways. Literature comparisons indicate that alternative synthesis approaches (*e.g.*, sol–gel, hydrothermal, ultrasonic-assisted methods) can significantly alter morphology, crystallite size, and defect chemistry, thereby impacting conductivity and dielectric behavior. Our results thus establish the solid-state method as a reliable baseline for correlating structural integrity with electrochemical performance in $LiVO_3$.

Given the potential toxicity of vanadium compounds, proper safety protocols must be followed during the synthesis, handling, and disposal of $LiVO_3$ to mitigate environmental and health risks. Future work will focus on systematically comparing different synthesis methods to further unravel the structure–property relationships and optimize $LiVO_3$ for potential energy storage and solid-state electrolyte applications.

## Author contributions

Leila Miladi: Writing – original draft, visualization, methodology, investigation, formal analysis. Saber Nasri: Writing – review & editing, software, methodology, investigation. Amnah M Alofi: Validation, supervision, resources, project administration, methodology. Manel Essid: Supervision, validation, project administration. Abderrazek Oueslati: Writing – original draft, supervision, methodology.

## Conflicts of interest

The authors declare that they have no known competing financial interests or personal relationships that could have appeared to influence the work reported in this paper.

## Data availability

Data will be made available on request.

## Acknowledgements

The authors extend their appreciation to the Deanship of Research and Graduate Studies at King Khalid University for funding this work through Large Research Project under grant number RGP2/148/46.

## References

1 Y. Qu, W. Tang, H. Liu, C. Li, L. Zou, Z. Chen, Z. Yang, J. Su and W. Zhang, Threefold Modification with Dual-Cation Doping and $LiVO_3$ Coating Boosts Long-Term Cyclability and Rate Capability of Li-Rich Cathode Materials for Lithium-Ion Batteries, *J. Ind. Eng. Chem. Res.*, 2023, **62**, 10467–10476, DOI: 10.1021/acs.iecr.3c00889.

2 A. Manthiram, A reflection on lithium-ion battery cathode chemistry, *J. Nat. Commun.*, 2020, **11**, 1550, DOI: 10.1038/s41467-020-15355-0.

3 X. Li, M. Ma, W. Lv, G. Wu, R. Lian, W. Zhang and Z. Li, Coordination interaction boosts energy storage in rechargeable Al battery with a positive electrode material of CuSe, *J.Chem. Eng.*, 2021, **421**, 127792, DOI: 10.1016/j.cej.2020.127792.

4 Z. Wang, Z. Du, L. Wang, G. He, I. P. Parkin, Y. Zhang and Y. Yue, Disordered materials for high-performance lithium-ion batteries: A review, *J. Nano Energy.*, 2024, **121**, 109250, DOI: 10.1016/j.nanoen.2023.109250.

5 D. Zhao, C. Dong, X. Pu, H. Huang, X. Fu and Z. Chen, Facile Synthesis of Porous Coralline LiVO3 as High-Performance Li-Ion Battery Cathodes, *J. ChemistrySelect*, 2018, **3**, 592–598, DOI: 10.1002/slct.201702962.

6 Z. Li, X. Feng, L. Mi, J. Zheng, X. Chen and W. Chen, Hierarchial porous onion-shaped $LiMn_2O_4$ as ultrahigh-rate cathode material for lithium ion batteries, *J. Nano Res.*, 2018, **11**, 4038–4048, DOI: 10.1007/s12274-018-1986-z.

7 Q. Liu, Z. F. Li, Y. Liu, H. Zhang, Y. Ren, C. J. Sun, W. Lu, Y. Zhou, L. Stanciu, E. A. Stach and J. Xie, Graphene-modified nanostructured vanadium pentoxide hybrids with extraordinary electrochemical performance for Li-ion batteries, *J. Nat. Commun.*, 2015, **6**, 6127, DOI: 10.1038/ncomms7127.

8 J. H. Yao, Z. L. Yin, Z. G. Zou and Y. W. Li, Y-doped $V_2O_5$ with enhanced lithium storage performance, *RSC Adv.*, 2017, **7**, 32327–32335, DOI: 10.1039/C7RA03885B.

Open Access Article. Published on 08 September 2025. Downloaded on 10/28/2025 4:06:54 PM.
This article is licensed under a Creative Commons Attribution-NonCommercial 3.0 Unported Licence.

9 R. Liang, Y. Du, P. Xiao, J. Cheng, S. Yuan, Y. Chen, J. Yuan and J. Chen, Transition Metal Oxide Electrode Materials for Supercapacitors: A Review of Recent Developments, *Nanomaterials.*, 2021, **11**, 1248, DOI: 10.3390/nano11051248.

10 M. Prześniak-Welenc, M. Nadolska, K. Jurak, J. Li, K. Górnicka, A. Mielewczyk-Gryń, M. Rutkowska and A. P. Nowak, The valance state of vanadium-key factor in the flexibility of potassium vanadates structure as cathode materials in Li-ion batteries, *Sci. Rep.*, 2022, **12**, 18751, DOI: 10.1038/s41598-022-23509-x.

11 T. N. Shinde, A. Vedpathak, B. J. Nagare, D. M. Sapkal, M. Desai, P. P. Atre and S. D. Sartale, 1D Layered $LiVO_3$ Nanorods Synthesized by Ultrasonic-Assisted Chemical Route for Supercapacitor Applications, *Energy Technol.*, 2024, **12**, 2301056, DOI: 10.1002/ente.202301056.

12 D. Yang, D. Zhang, H. Wu, T. Xiao and S. Ni, A novel approach to $LiVO_3$ synthesis enables its outstanding lithium storage performance, *Ionics*, 2022, **28**, 3671–3678, DOI: 10.1007/s11581-022-04637-w.

13 J. Pan, P. Zhao, N. Wang, F. Huang and S. Dou, Research progress in stable interfacial constructions between composite polymer electrolytes and electrodes, *Energy Environ. Sci.*, 2022, **15**, 2753, DOI: 10.1039/d1ee03466a.

14 Y. Jung, J. E. Mueller, S. Chaikasetsin, G. D. Han, S. Nie, H. S. Han, T. M. Gür and F. B. Prinz, Mixed Conducting Oxide Coating for Lithium Batteries, *ACS Nano*, 2025, **19**(1), 1783–1793, DOI: 10.1021/acsnano.4c16117.

15 M. Zhao, X. Wu and Y. Bando, Structural optimization of VO2/NH4V4O10 cathode materials for high-performance wide-temperature zinc-ion, *Inorg. Chem. Front.*, 2025, DOI: 10.1039/D5QI01098E.

16 R. Baddour-Hadjean, A. Boudaoud, S. Bach, N. Emery and J. P. Pereira-Ramos, A comparative insight of potassium vanadates as positive electrode materials for li batteries: Influence of the long-range and local structure, *Inorg. Chem.*, 2014, **53**, 1764–1772, DOI: 10.1021/ic402897d.

17 M. Jian, J. P. Tu, Y. Q. Qiao, Y. Lu, X. L. Wang and C. D. Gu, Synthesis and electrochemical performance of LiVO3 cathode materials for lithium ion batteries, *J. Power Sources*, 2013, **236**(15), 33–38, DOI: 10.1016/j.jpowsour.2013.02.004.

18 Y. Chen, C. Chen, W. Chen, H. Liu and J. Zhu, Influence of thermal-decomposition temperatures on structures and properties of V2O5 as cathode materials for lithium ion battery, *Prog. Nat. Sci.:Mater. Int.*, 2015, **25**, 42–46, DOI: 10.1016/j.pnsc.2015.01.004.

19 I. T. Adebanjo, J. Eko, A. G. Agbeyegbe, S. F. Yuk, S. V. Cowart, E. A. Nagelli, F. J. Burpo, J. L. Allen, D. T. Tran, N. Bhattarai, K. Shah, J.-Y. Hwang and H. H. Sun, A comprehensive review of lithium-ion battery components degradation and operational considerations: a safety perspective, *Energy Adv.*, 2025, **4**, 820–877, DOI: 10.1039/D5YA00065C.

20 Z. Chen, L. Cao, L. Chen, H. Zhou, K. Xieb and Y. Kuang, Nanoplate-stacked baguette-like $LiVO_3$ as a high performance cathode material for lithium-ion batteries, *J. Mater. Chem. A*, 2015, **3**, 8750, DOI: 10.1039/c5ta00928.

21 L. Miladi, N. Ben Hamadi, A. Oueslati, A. Guesmi, F. Boufahja and H. Naïli, Structural and electrical properties of Li- and Na-Based chromium NASICON: Insights into ionic conductivity and dielectric behavior, *Inorg. Chem. Commun.*, 2025, **177**, 114391, DOI: 10.1016/j.inoche.2025.114391.

22 S. B. R. S Adnan and N. S. Mohamed, Conductivity and Dielectric Studies of $Li_2ZnSiO_4$ Ceramic Electrolyte Synthesized *via* Citrate Sol Gel Method, *Int. J. Electrochem. Sci.*, 2012, **7**, 9844–9858, DOI: 10.1016/S1452-3981(23)16242-0.

23 L. Singh, U. S. Rai and K. D. Mandal, Dielectric, modulus and impedance spectroscopic studies of nanostructured $CaCu_{2.70}Mg_{0.30}Ti_4O_{12}$ electro-ceramic synthesized by modified sol–gel route, *J. Alloys Compd.*, 2013, **555**, 176–183, DOI: 10.1016/j.jallcom.2012.12.023.

24 I. Elhamdi, F. Mselmi, H. Souissi, S. Kammoun, E. Dhahri, P. Sanguinob and B. F. O. Costa, Summerfield scaling model and electrical conductivity study for understanding transport mechanisms of a $Cr^{3+}$ substituted $ZnAl_2O_4$ ceramic, *RSC Adv.*, 2023, **13**, 3377, DOI: 10.1039/d2ra07701a.

25 T. Šalkus, E. Kazakevičius, A. Kežionis, A. F. Orliukas, J. C. Badot and O. Bohnke, Determination of the non-Arrhenius behaviour of the bulk conductivity of fast ionic conductors LLTO at high temperature, *Solid State Ionics*, 2011, **188**, 69–72, DOI: 10.1016/j.ssi.2010.09.005.

26 A. K. Panda, L. Sahoo, N. C. Nayak, B. N. Parida and R. K. Parida, Structural and electrical analysis of polycrystalline ceramic $PbCaBiNbO_6$, *J. Mater. Sci.: Mater. Electron.*, 2023, **34**, 1640, DOI: 10.1007/s10854-023-11045-x.

27 G. Della Ventura, F. Galdenzi, A. Marcelli, G. Cibin, R. Oberti, F. C. Hawthorne, S. Bernardini and B. Mihailova, In situ simultaneous Fe K-edge XAS spectroscopy and resistivity measurements of riebeckite: Implications for anomalous electrical conductivity in subduction zones, *Geochem. J.*, 2024, **84**, 126037, DOI: 10.1016/j.chemer.2023.126037.

28 G. Della Ventura, F. Galdenzi, A. Marcelli, G. Cibin, R. Oberti, F. C. Hawthorne, S. Bernardini and B. Mihailova, In situ simultaneous Fe K-edge XAS spectroscopy and resistivity measurements of riebeckite: Implications for anomalous electrical conductivity in subduction zones, *Geochem. J.*, 2024, **84**, 126037, DOI: 10.1016/j.chemer.2023.126037.

29 I. Garoui, N. BenHamadi, S. Nasri, A. Oueslati, A. Guesmi, L. Khezami and H. Naïli, Dielectric relaxation and electrothermal charge carrier transport *via* correlated barrier hopping in the solid electrolyte $TlFeP_2O_7$: Experimental and theoretical modeling, *Ceram. Int*, 2025, **51**(19), 29510–29525, DOI: 10.1016/j.ceramint.2025.04.155.

30 The bulk DC conductivity (σ_dc) of LiVO3 was extracted from impedance spectroscopy measurements by using the bulk resistance (R) obtained from the equivalent circuit fitting, with the following relation.

31 U. Akgula, Z. Erginb, M. Sekercib and Y. Atici, AC conductivity and dielectric behavior of $[Cd(phen)_2(SCN)_2]$,

 © 2025 The Author(s). Published by the Royal Society of Chemistry

Open Access Article. Published on 08 September 2025. Downloaded on 10/28/2025 4:06:54 PM. This article is licensed under a Creative Commons Attribution-NonCommercial 3.0 Unported Licence.

*J. Vac. Sci. Technol.*, 2008, **82**, 340–345, DOI: 10.1016/j.vacuum.2007.05.001.

32 B. Huang, B. Xu, J. Zhang, Z. Li, Z. Huang, Y. Li and C. A. Wang, Li-ion conductivity and stability of hot-pressed LiTa2PO8 solid electrolyte for all-solid-state batteries Bing, *J. Mater. Sci.*, 2021, **56**, 2425–2434, DOI: 10.1007/s10853-020-05324-9.

33 R. Chtourou, B. Louati and K. Guidara, AC and DC conductivity study of $KPb_4(PO_4)_3$ compound using impedance spectroscopy, *J. Alloys Compd.*, 2017, **727**, 771, DOI: 10.1016/j.jallcom.2017.08.163.

34 R. Chtourou, B. Louati and K. Guidara, AC and DC conductivity study of $KPb_4(PO_4)_3$ compound using impedance spectroscopy, *J. Alloys Compd.*, 2017, **727**, 771, DOI: 10.1016/j.jallcom.2017.08.163.

35 M. A. Morsi, A. I. Al-Sulami, F. M. H. Al Sulami, M. O. Farea, M. A. Alqarni, A. A. Alhazime and A. Rajeh, Preparation, structural characterization, optical, photoluminescence, AC electrical conductivity and broadband dielectric properties of $WO_3$ reinforced PEG/CS blend for futuristic optoelectronic and energy storage devices, *Results Phys.*, 2024, **59**, 107582, DOI: 10.1016/j.rinp.2024.107582.

36 S. R. Elliott, Temperature dependence of a.c. conductivity of chalcogenide glasses, *Philos. Mag. B*, 1978, **37**, 553–560.

37 S. Nasri, M. Megdiche and M. Gargouri, Electrical conduction and dielectric properties of a newly synthesized single phase: $Ag_{0.4}Na_{0.6}FeP_2O_7$, *Phys. B*, 2014, **451**(15), 120–127, DOI: 10.1016/j.physb.2014.06.036.

38 M. Megdiche, C. Perrin-pellegrino and M. Gargouri, Conduction mechanism study by overlapping large-polaron tunnelling model in SrNiP2O7 ceramic compound, *J. Alloys Compd.*, 2014, **584**, 209–215, DOI: 10.1016/j.jallcom.2013.09.021.

39 A. K. Jonscher, *Dielectric Relaxation in Solids*, Chelsea Dielectrics Press, London (1983).

40 Y. Wang, J. Song, J. Xia, T. Chen and J. Dong, Small polaron hopping conduction in $LiCoO_2$ cathode materials, *J. Electrochem. Soc.*, 2018, **165**(10), A1608–A1615, DOI: 10.1149/2.0341810jes.

41 S. Aydi, S. Chkoundali, A. Oueslati and A. Aydi, Effect of lithium doping on the structural, conduction mechanism and dielectric property of MnNbO4, *RSC Adv.*, 2023, **13**, 20093–20104, DOI: 10.1039/D3RA03393G.

42 S. Han, J. Park, W. Lu and A. M. Sastry, Numerical study of grain boundary effect on $Li^+$ effective diffusivity and intercalation-induced stresses in Li-ion battery active materials, *J. Power Sources*, 2013, **240**(15), 155–167, DOI: 10.1016/j.jpowsour.2013.03.135.

43 I. Ragbaoui, S. Aydi, S. Chkoundali, M. Enneffati and A. Aydi, Effect of substitution on the structural, electrical properties, and dielectric relaxor behavior in lead- free $BiFeO_3$-based ceramics, *RSC Adv.*, 2024, **14**, 1330, DOI: 10.1039/d3ra06962a.

44 A. Rafik, E. Abderrahmane, O. Dagdag, H. Kim, H. Zouihri, E. Sabbar and T. Guedira, Investigation of hybrid phosphate by complex impedance spectroscopy, *J. Chem. Phys.*, 2024, **8**, 100590, DOI: 10.1016/j.chphi.2024.100590.

45 R. Kumar and R. Kumar, Structural and dielectric properties of $Sr^{2+}$ ions substituted $NdCrO_3$ orthochromate perovskite, *Appl. Phys.*, 2023, **129**, 832, DOI: 10.1007/s00339-023-07093-z.

46 S. K. Barik, R. N. P. Choudhary and A. K. Singh, Ac impedance spectroscopy and conductivity studies of Ba0.8Sr0.2TiO3 ceramics, *Adv. Mater. Lett.*, 2011, **2**, 419–424, DOI: 10.5185/amlett.2011.2228.

47 N. Kaur, M. Singh, L. Singh, A. M. Awasthi and S. P. Lochab, Dielectric relaxation of gamma irradiated muscovite mica, *Mater. Res. Bull.*, 2015, **63**, 24–31, DOI: 10.1016/j.materresbull.2014.11.034.MRB.7846.

48 M. Ram, Structure and electrical conduction behavior of $LiZnVO_4$ ceramic prepared by solution-based chemical route, *J. Alloys Compd.*, 2011, **509**, 5688–5691, DOI: 10.1016/j.jallcom.2011.02.128.

49 R. Fouad, T. E. Ali, b M. A. Assirib and S. S. Shenouda, Synthesis, structural, spectroscopic and electric/dielectric studies of a nanocrystalline Ni(II) complex based on [(1,3-diphenyl-1H-pyrazol-4-yl) methylene]thiocarbonohydrazide, *RSC Adv.*, 2024, **14**, 9747, DOI: 10.1039/d4ra00665h.

50 O. Rejaiba, F. Hcini, M. Nasri, B. Alzahrani, M. L. Bouazizi, E. K. Hlil, J. Khelifi, K. Khirouni and E. Dhahri, Structural, dielectric and electrical properties of Sol–gel auto-combustion technic of $CuFeCr_{0.5}Ni_{0.5}O_4$ ferrite, *J. Mater. Sci.*, 2021, **56**, 16044–16058, DOI: 10.1007/s10853-021-06315-0.

51 W. Jilani, A. Bouzidi, K. Omri, M. Al-Dossari, I. S. Yahia and H. Guermazi, A free-standing Co: ZnO (CZO) doped PVA nanocomposite polymer system films (CZO-PVA NCPSFs) for optical sensing electronic devices, *J. Phys. B: At. Mol. Opt. Phys.*, 2023, **666**, 415128.

52 S. Karmakar, H. Tyagi, D. P. Mohapatra and D. Behera, Dielectric relaxation behavior and overlapping large polaron tunneling conduction mechanism in NiOePbO m-cauliflower composites, *J. Alloys Compd.*, 2021, **851**, 156789, DOI: 10.1016/j.jallcom.2020.

53 A. Daidouh, M. L. Veiga and C. Pico, Structure Characterization and Ionic Conductivity of $Ag_2VP_2O_8$, *J. Solid State Chem.*, 1997, **130**, 28–34, DOI: 10.1006/jssc.1996.7266.

54 M. Madani, S. Mnefgui and K. Omri, Synthesis and Comprehensive Characterization of Sr2TiZrO6 Double Perovskite: Insights into Dielectric and Electrical Properties for Advanced Applications, *J. Inorg. Organomet. Polym. Mater.*, 2025, DOI: 10.1007/s10904-025-03696-6.

55 F. Tayari, S. S. Teixeira, M. P. F. Graca and K. I. Nassar, A Comprehensive Review of Recent Advances in Perovskite Materials: Electrical, Dielectric, and Magnetic Properties, *Inorganics*, 2025, **13**, 67, DOI: 10.3390/inorganics13030067.

56 M. Y. Gneber, I. Elhamdi, J. Messoudi, Ra. Dhahri, F. Sahnoune, M. Jemmali, M. Hussein, Es. Dhahri and B. F. O. Costa, Investigation of variable range hopping and dielectric relaxation in $GdCrO_3$ orthochromite perovskites, *RSC Adv.*, 2024, **14**, 36161, DOI: 10.1039/d4ra06104g.

57 J. Zhang, W. Li, J. Yang, W. Wang, J. Wang, Q. Dong, X. Wang, Y. Wu, Y. Xu, Y. Wang, H. Yang, N. Wang, Y. Ren and X. Li, Enabling Quasi-Zero-Strain Behavior of Layered

Open Access Article. Published on 08 September 2025. Downloaded on 10/28/2025 4:06:54 PM.
This article is licensed under a Creative Commons Attribution-NonCommercial 3.0 Unported Licence.

Oxide Cathodes *via* Multiple-cations Induced Order-to-Disorder Transition, *Small*, 2024, **20**, 2404099, DOI: 10.1002/smll.202404099.

58 J. Zhang, W. Li, J. Yang, J. Wang, Q. Dong, X. Wang, Y. Wu and Y. Ren, Interlayer Entropy Engineering Inducing the Symmetry-Broken Layered Oxide Cathodes to Activate Reversible High-Voltage Redox Reaction, *Small*, 2024, **20**, 2401443, DOI: 10.1002/smll.202401443.

59 J. Zhang, W. Li, J. Wang, X. Pu, G. Zhang, S. Wang, N. Wang and X. Li, Engineering p-Band Center of Oxygen Boosting H+ Intercalation in δ-MnO2 for Aqueous Zinc Ion Batteries, *Angew. Chem., Int. Ed.*, 2024, **135**, e202215654, DOI: 10.1002/anie.202215654.

60 Z. Huang, L. Cao, L. Chen, Y. Kuang, H. Zhou, C. Fu and Z. Chen, Preparation, Characterization, and Lithium Intercalation Behavior of LiVO3 Cathode Material for Lithium-Ion Batteries, *J. Phys. Chem. C*, 2016, **120**(6), 3242–3249, DOI: 10.1021/acs.jpcc.5b12666.

61 H. Zhao, L. Liu, X. Zhang, R. Gao, Z. Hu and X. Liu, Facile synthesis of carbon-coated $LiVO_3$ with enhanced electrochemical performances as cathode materials for lithium-ion batteries, *Ceram. Int.*, 2017, **43**(2), 2343–2349, DOI: 10.1016/j.ceramint.2016.10.209.

62 X. M. Jian, J. P. Tu, Y. Q. Qiao, Y. Lu, X. L. Wang and C. D. Gu, Synthesis and electrochemical performance of LiVO3 cathode materials for lithium ion batteries, *J. Power Sources*, 2013, **236**(15), 33–38, DOI: 10.1016/j.jpowsour.2013.02.004.

63 S. Li, Y. F. Zhang, Y. Tang, X. P. Tan, S. Q. Liang and J. Zhou, Facile synthesis of LiVO3 and its electrochemical behavior in rechargeable lithium batteries, *J. Electroanal. Chem.*, 2019, **853**(15), 113505, DOI: 10.1016/j.jelechem.2019.113505.

64 D. Yang, D. Zhang and H. Wu, A novel approach to LiVO3 synthesis enables its outstanding lithium storage performance, *Ionics*, 2022, **28**(15), 3671–3678, DOI: 10.1007/s11581-022-04637-w.

 © 2025 The Author(s). Published by the Royal Society of Chemistry